

REPORT DOCUMENTATION PAGE			Form Approved OMB NO. 0704-0188		
<p>The public reporting burden for this collection of information is estimated to average 1 hour per response, including the time for reviewing instructions, searching existing data sources, gathering and maintaining the data needed, and completing and reviewing the collection of information. Send comments regarding this burden estimate or any other aspect of this collection of information, including suggestions for reducing this burden, to Washington Headquarters Services, Directorate for Information Operations and Reports, 1215 Jefferson Davis Highway, Suite 1204, Arlington VA, 22202-4302. Respondents should be aware that notwithstanding any other provision of law, no person shall be subject to any penalty for failing to comply with a collection of information if it does not display a currently valid OMB control number.</p> <p>PLEASE DO NOT RETURN YOUR FORM TO THE ABOVE ADDRESS.</p>					
1. REPORT DATE (DD-MM-YYYY)		2. REPORT TYPE New Reprint		3. DATES COVERED (From - To) -	
4. TITLE AND SUBTITLE Linear Friction Welding Process Model for Carpenter Custom 465 Precipitation-Hardened Martensitic Stainless Steel			5a. CONTRACT NUMBER W911NF-11-1-0207		
			5b. GRANT NUMBER		
			5c. PROGRAM ELEMENT NUMBER 622105		
6. AUTHORS R. Yavari, J. S. Snipes, S. Ramaswami, C. -F. Yen, B. A. Cheeseman, M. Grujicic			5d. PROJECT NUMBER		
			5e. TASK NUMBER		
			5f. WORK UNIT NUMBER		
7. PERFORMING ORGANIZATION NAMES AND ADDRESSES Clemson University 300 Brackett Hall Box 345702 Clemson, SC 29634 -5702			8. PERFORMING ORGANIZATION REPORT NUMBER		
9. SPONSORING/MONITORING AGENCY NAME(S) AND ADDRESS (ES) U.S. Army Research Office P.O. Box 12211 Research Triangle Park, NC 27709-2211			10. SPONSOR/MONITOR'S ACRONYM(S) ARO		
			11. SPONSOR/MONITOR'S REPORT NUMBER(S) 57228-EG.29		
12. DISTRIBUTION AVAILABILITY STATEMENT Approved for public release; distribution is unlimited.					
13. SUPPLEMENTARY NOTES The views, opinions and/or findings contained in this report are those of the author(s) and should not be construed as an official Department of the Army position, policy or decision, unless so designated by other documentation.					
14. ABSTRACT An Arbitrary Lagrangian-Eulerian finite-element analysis is combined with thermo-mechanical material constitutive models for Carpenter Custom 465 precipitation-hardened martensitic stainless steel to develop a linear friction welding (LFW) process model for this material. The main effort was directed toward developing reliable material constitutive models for Carpenter Custom 465 and toward improving functional relations and parameterization of the workpiece/workpiece contact-interaction models. The LFW process model is then used to predict thermo-mechanical response of Carpenter Custom 465 during LFW.					
15. SUBJECT TERMS Carpenter Custom 465 precipitation-hardened martensitic stainless steel, linear friction welding, process modeling					
16. SECURITY CLASSIFICATION OF:			17. LIMITATION OF ABSTRACT UU	15. NUMBER OF PAGES	19a. NAME OF RESPONSIBLE PERSON Mica Grujicic
a. REPORT UU	b. ABSTRACT UU	c. THIS PAGE UU			19b. TELEPHONE NUMBER 864-656-5639

## **Report Title**

Linear Friction Welding Process Model for Carpenter Custom 465 Precipitation-Hardened Martensitic Stainless Steel

### **ABSTRACT**

An Arbitrary Lagrangian-Eulerian finite-element analysis is combined with thermo-mechanical material constitutive models for Carpenter Custom 465 precipitation-hardened martensitic stainless steel to develop a linear friction welding (LFW) process model for this material. The main effort was directed toward developing reliable material constitutive models for Carpenter Custom 465 and toward improving functional relations and parameterization of the workpiece/workpiece contact-interaction models. The LFW process model is then used to predict thermo-mechanical response of Carpenter Custom 465 during LFW. Specifically, temporal evolutions and spatial distribution of temperature within, and expulsion of the workpiece material from, the weld region are examined as a function of the basic LFW process parameters, i.e., (a) contact-pressure history, (b) reciprocation frequency, and (c) reciprocation amplitude. Examination of the results obtained clearly revealed the presence of three zones within the weld, i.e., (a) Contact-interface region, (b) Thermo-mechanically affected zone, and (c) heat-affected zone. While there are no publicly available reports related to Carpenter Custom 465 LFW behavior, to allow an experiment/computation comparison, these findings are consistent with the results of our ongoing companion experimental investigation.

---

## REPORT DOCUMENTATION PAGE (SF298) (Continuation Sheet)

---

Continuation for Block 13

ARO Report Number 57228.29-EG  
Linear Friction Welding Process Model for Carpt..

Block 13: Supplementary Note

© 2014 . Published in Journal of Materials Engineering and Performance, Vol. Ed. 0 23, (6) (2014), (, (6). DoD Components reserve a royalty-free, nonexclusive and irrevocable right to reproduce, publish, or otherwise use the work for Federal purposes, and to authroize others to do so (DODGARS §32.36). The views, opinions and/or findings contained in this report are those of the author(s) and should not be construed as an official Department of the Army position, policy or decision, unless so designated by other documentation.

Approved for public release; distribution is unlimited.

# Linear Friction Welding Process Model for Carpenter Custom 465 Precipitation-Hardened Martensitic Stainless Steel

M. Grujicic, R. Yavari, J.S. Snipes, S. Ramaswami, C.-F. Yen, and B.A. Cheeseman

(Submitted November 11, 2013; in revised form January 31, 2014; published online April 11, 2014)

An Arbitrary Lagrangian-Eulerian finite-element analysis is combined with thermo-mechanical material constitutive models for Carpenter Custom 465 precipitation-hardened martensitic stainless steel to develop a linear friction welding (LFW) process model for this material. The main effort was directed toward developing reliable material constitutive models for Carpenter Custom 465 and toward improving functional relations and parameterization of the workpiece/workpiece contact-interaction models. The LFW process model is then used to predict thermo-mechanical response of Carpenter Custom 465 during LFW. Specifically, temporal evolutions and spatial distribution of temperature within, and expulsion of the workpiece material from, the weld region are examined as a function of the basic LFW process parameters, i.e., (a) contact-pressure history, (b) reciprocation frequency, and (c) reciprocation amplitude. Examination of the results obtained clearly revealed the presence of three zones within the weld, i.e., (a) Contact-interface region, (b) Thermo-mechanically affected zone, and (c) heat-affected zone. While there are no publicly available reports related to Carpenter Custom 465 LFW behavior, to allow an experiment/computation comparison, these findings are consistent with the results of our ongoing companion experimental investigation.

**Keywords** Carpenter Custom 465 precipitation-hardened martensitic stainless steel, linear friction welding, process modeling

## 1. Introduction

Linear friction welding (LFW) falls into the category of solid-state frictional-sliding-based joining processes. As schematically shown in Fig. 1, the LFW process involves (relative) reciprocating linear motion of the two workpieces to be joined. As a result of frictional sliding, heat is dissipated at the faying/contacting flat surfaces, promoting material softening in the surrounding region, plastic deformation, material expulsion, and ultimate adhesion/bonding.

Detailed past investigations of LFW (Ref 1-3) established the presence of five distinct phases of this joining process: (a) initial phase, (b) transition phase, (c) equilibrium phase, (d) deceleration/forging phase, and (e) stand phase. A simple schematic of the first four phases is depicted in Fig. 2. Since the last phase does not involve workpiece length-scale structural/kinematic effects, it is not shown. Considering the fact that the defining features of the five LFW phases can be found in Ref 1-3, they will not be repeated here.

M. Grujicic, R. Yavari, J.S. Snipes, and S. Ramaswami, Department of Mechanical Engineering, Clemson University, 241 Engineering Innovation Building, Clemson, SC 29634-0921; and C.-F. Yen and B.A. Cheeseman, Army Research Laboratory – Survivability Materials Branch, Aberdeen, Proving Ground, MD 21005-5069. Contact e-mail: gmica@clemson.edu.

The main LFW process parameters can be defined as follows: (a) alloy-grade and thermal-mechanical treatment of the workpiece materials to be joined, (b) frequency of reciprocating motion, (c) amplitude of reciprocating motion, (d) temporal variation of contact/upsetting/forging pressure, (e) total duration of LFW process, and (f) the geometry of the contacting surfaces. It is generally accepted that selection of these parameters (or more precisely, their combination) may have a profound effect on the structural integrity and quality of the resulting weld.

A detailed account of the main advantages of LFW relative to the other friction-based welding processes, solid-state joining processes, and fusion-based welding processes can be found in Ref 4. The same reference also provides a detailed description of the key limitations, as well as the main areas of application, of this joining process.

Examination of the open-domain literature carried out as part of the present work identified a number of investigations demonstrating successful application of the LFW process to join various metal-alloy grades such as (a) titanium alloys [e.g., (Ref 5-8)], (b) superalloys (Ref 9), (c) steels (Ref 10, 11), and (d) intermetallics (Ref 12). Cumulatively, these investigations established that the temperature in the contact region plays a dominant role in the joining process, affecting the phenomena such as welding efficiency, spatial distribution, and temporal evolution of material deformation and microstructure fields, as well as quality/structural integrity of the weld.

The work presented in this manuscript deals with LFW of Carpenter Custom 465 precipitation-hardened martensitic stainless steel. This material is being considered for use in aircraft-structure applications, and LFW is being considered as the main joining-process candidate. However, no reports pertaining to

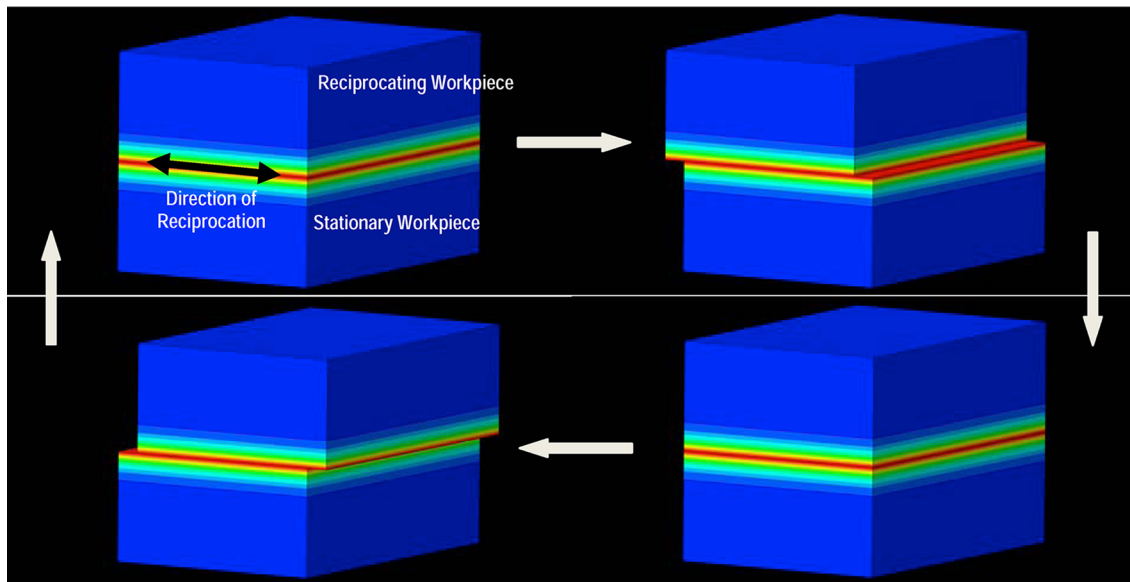


**Fig. 1** A schematic of a single cycle of the Linear Friction Welding (LFW) process

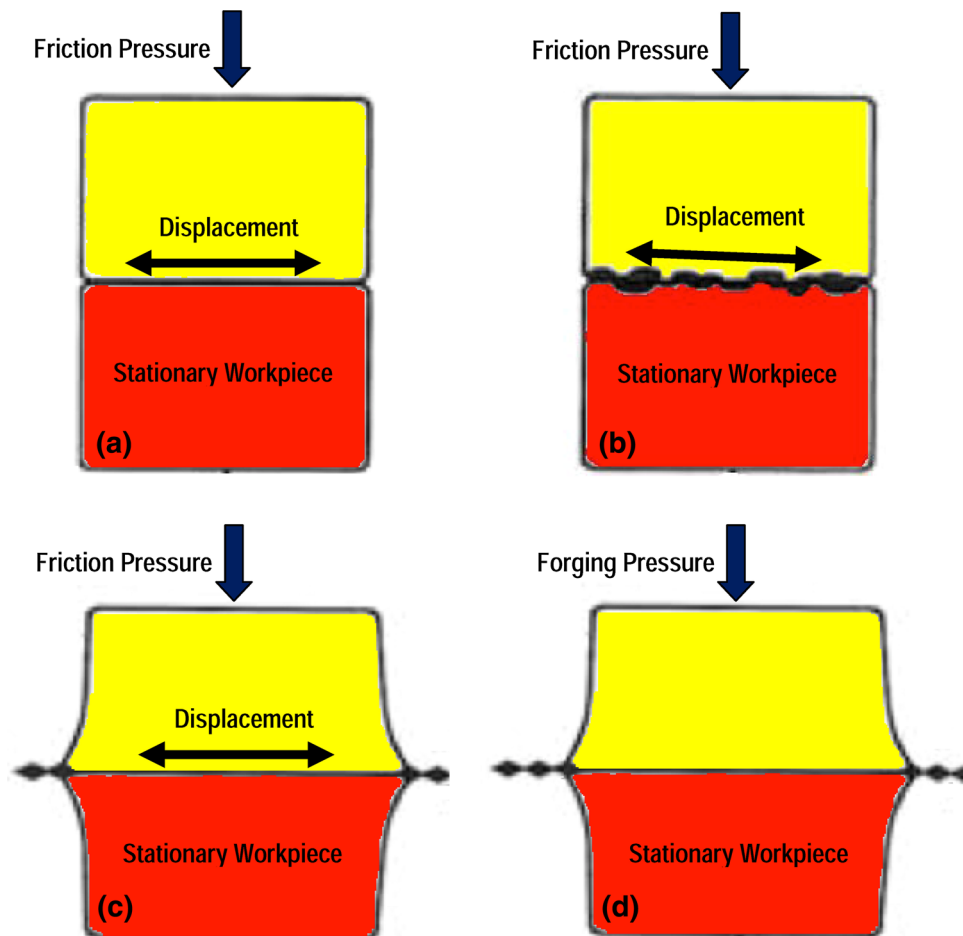


**Fig. 2** First four phases of the LFW process: (a) initial phase, (b) transition phase, (c) equilibrium phase, and (d) deceleration/forging phase

LFW of this material could be found in the open literature. The present work tries to fill this void through the development, parameterization, and validation of an LFW process model.

The material closest to Carpenter Custom 465 for which an experimental LFW investigation has been reported is AISI 316L, a low-carbon austenitic stainless steel (Ref 13). The work

presented in Ref 13 established three important points: (a) through proper selection of the LFW process parameters, sound/ flaw-free welds can be produced; (b) again through proper selection of the process parameters, the development of undesirable microstructures within different weld zones can be avoided. For example, by selecting the process parameters to maximize the burn-off rate (i.e., the rate at which plasticized material is expelled from the contact region), formation of the undesirable  $\delta$ -ferrite can be prevented in the weld region; and (c) determination of the optimum process parameters using purely experimental means relies on the post-mortem (typically destructive) examination of the LFW joints.

As established above, a purely experimental approach to the LFW process suffers from a number of shortcomings related to the real-time determination of the (optimal) process parameters and the weld conditions (e.g., temperature distribution over the contact surface and in the direction normal to it), microstructure distribution throughout the weld region, etc. These shortcomings can be potentially overcome through the use of high-fidelity LFW process models. An overview of the public-domain literature revealed the following LFW modeling and simulation studies which appear the most noteworthy: (a) a two-dimensional fully coupled thermo-mechanical finite-element model of the LFW process has been developed by D'Alvise et al. (Ref 14), who employed an innovative adaptive contact and re-meshing algorithm to simulate flash formation. However, due to the two-dimensional character of the process model, full validation of the model against the available experimental data was associated with a number of challenges; (b) a three-dimensional fully coupled thermo-mechanical finite-element model for the LFW process has been developed by Sorina-Muller et al. (Ref 15), who applied it to Ti-6Al-2Sn-4Cr-6Mo alloy weldments. While the computed results and the corresponding experimental data related to the temporal evolution of the axial shortening and the spatial distribution of microhardness in the as-welded material state are claimed to be in very good agreement, the constitutive model for the subject material was fairly simple and did not properly reflect many aspects of the material mechanical response under dynamic, elevated-temperature, and high-contact-pressure loading conditions; and (c) the model of Sorina-Muller et al. (Ref 15) has been extended by Grujicic et al. (Ref 16) in order to remove the aforementioned material-model shortcomings and provide a deeper insight into the development of material microstructure (and the associated mechanical properties) within different weld regions and their dependence on the LFW process parameters. Specifically, since the HAZ of the weld has been found to possess somewhat inferior mechanical properties relative to the TMAZ and the base metal, particular attention has been given to the problem of establishing processing/microstructure/property relations in this weld region. The model predictions and their experimental counterparts pertaining to the overall structural performance of the LFW joint are found to be in reasonably good agreement.

The main objective of the present work is to develop, parameterize, and validate an LFW process model for Carpenter Custom 465. Since a thermo-mechanical constitutive model for this material is not presently available in the open literature, a major effort in this work will be directed toward the development, parameterization, and validation of the appropriate material model. In addition, since contact interactions of the workpieces to be joined play a key role in the LFW-joint formation and the accompanying changes in the material

microstructure, considerable effort will also be directed toward improving the contact models and their parameterization.

## 2. Carpenter Custom 465

As mentioned earlier, the material analyzed in the present work is the premium (i.e., double vacuum)-melted Carpenter Custom 465 precipitation-hardened martensitic stainless (i.e., oxidation- and corrosion-resistant) steel (Ref 17). In this steel, improved oxidation resistance is achieved through the addition of chromium (minimum ca. 12 wt.%) which ensures formation of a continuous  $\text{Cr}_2\text{O}_3$ -based oxide protective surface film (with low-oxygen permeability and high adhesion strength). Enhanced corrosion resistance, on the other hand, is achieved by ensuring, through the chemical composition and heat treatment, that the matrix contains only one crystalline phase (i.e., martensite, in the present case). In (precipitation-hardened) Carpenter Custom 465, the requirement for increased fracture toughness and for the enhanced retention of mechanical properties at high temperatures demands the introduction of a secondary/precipitate phase (using an aging heat treatment). To ensure high resistance toward “dissimilar-metal” corrosion (i.e., corrosion between the matrix and the precipitate phases), the two phases are designed to have a small electronegativity difference. This is achieved by ensuring that the precipitate phase is of an intermetallic character (Ref 18).

### 2.1 Heat Treatment(s)

Carpenter Custom 465 with the temper designation H900 or H1000 is typically used in aircraft frames. It is, hence, the LFW of these Carpenter Custom 465 tempers that is analyzed in the present work. The H900/1000 heat treatment involves the following three steps:

- (a) *Solutionizing heat treatment*—Within this step, the material is first subjected to high temperatures (e.g., 1255 K/ 1 h), to convert its as-received microstructure into austenite, and then quenched to room temperature (to prevent diffusion-type decomposition of austenite). Since the room temperature is between the temperatures for the start and finish of the martensitic transformation (the so-called  $M_s$  and  $M_f$  temperatures, respectively), the as-quenched material consists of untransformed austenite and martensite;
- (b) *Cold-Treating*—In this step, the as-quenched material is, within a time period of less than 24 h following the solutionizing treatment, subjected to a refrigeration treatment at 200 K for about eight hours. Since  $M_f$  is higher than this temperature, austenite-to-martensite conversion continues until (near) completion. Subsequently, the material is allowed to warm to room temperature. The resulting fully martensitic structure contains numerous lath interfaces and intra-lath dislocations, and so provides an abundance of potential nucleation sites for the precipitate phase(s). This, in turn, ensures that during the subsequent aging treatment, the resulting microstructure will contain a high number density of very fine (material-property-enhancing) precipitates; and
- (c) *Aging Heat Treatment*—In this step, the annealed, quenched, and refrigeration-treated material is aged in a

temperature range between 755 and 894 K for four to eight hours. This is followed by a water or oil quench of the material. The resulting as-aged material condition is designated as Hxxx, where xxx is replaced with the aging temperature expressed in °F (e.g., H1000). A trade-off in material strength, fracture toughness, and stress-corrosion-cracking resistance in aged Carpenter Custom 465 (Ref 19), caused by differences in the aging temperature, are demonstrated in Fig. 3(a-c). It is seen that as the aging temperature increases, material strength decreases, Fig. 3(a), while its fracture toughness, Fig. 3(b), and stress-corrosion-cracking resistance, Fig. 3(c), increase. These results suggest that the exposure of the material within the weld to high temperatures can result in over-aging and, thus, in the (generally undesirable) loss of strength.

## 2.2 Precipitation Reaction(s) During Aging

In the course of the aging treatment of Carpenter Custom 465, coherent hexagonal-structure needle-shaped (material-strength-controlling)  $\omega$ -phase precipitates are first formed. As the aging temperature/duration is increased, and the material begins to over-age, these precipitates gradually become replaced by incoherent orthorhombic-structure plate-like  $\text{Ni}_3(\text{Ti},\text{Mo})$  precipitates. These microstructural changes are accompanied by a loss of material strength and, initially, an improvement in its fracture toughness. At sufficiently high aging temperatures, martensite-to-austenite reversion may take place, giving rise to a severe loss of material strength (a highly undesirable effect) and an increase in ductility. Changes in the microstructure of the material within the weld in Carpenter Custom 465 are currently being investigated in our ongoing

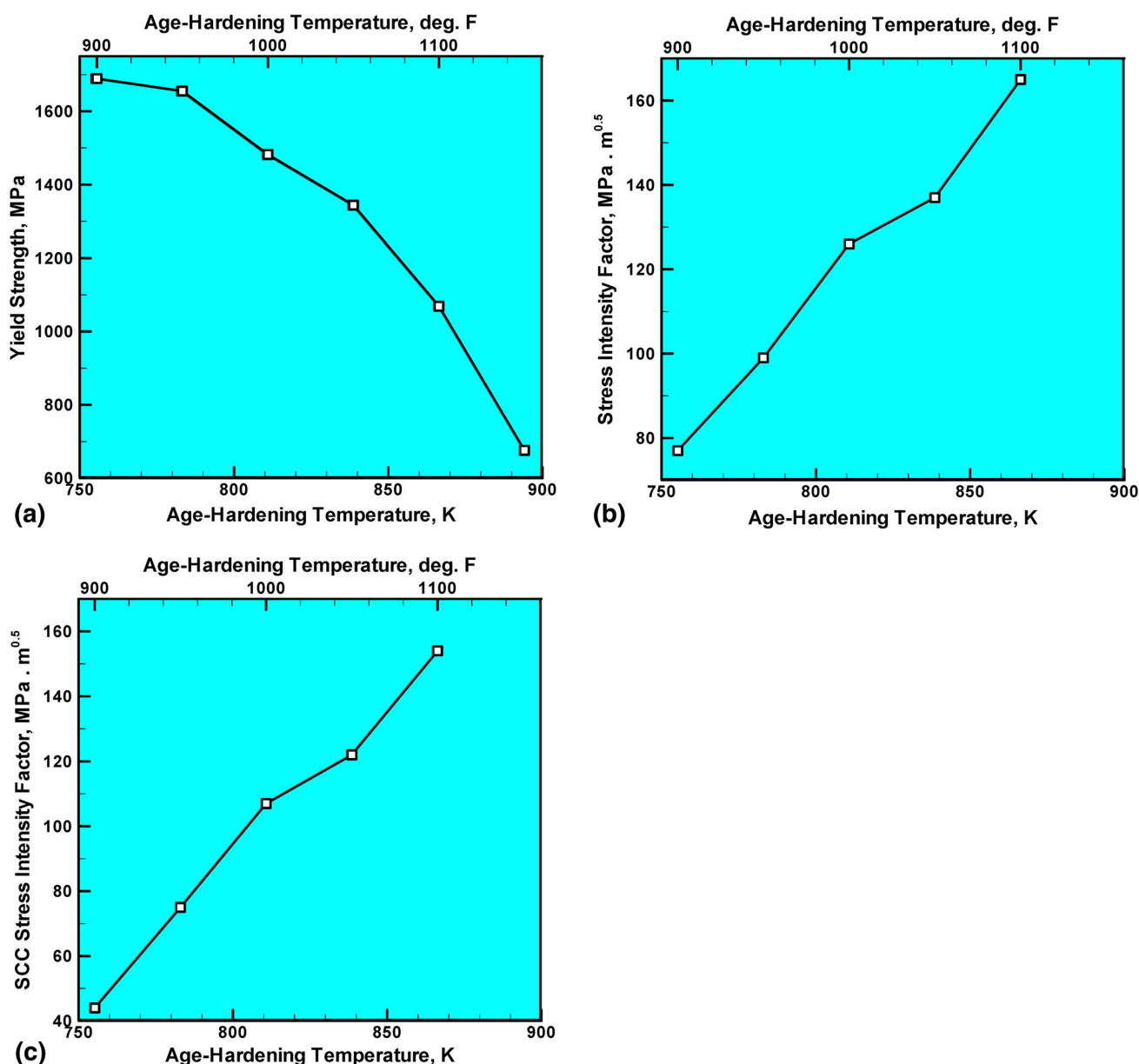


Fig. 3 The effect of aging temperature on the material (a) yield strength, (b) fracture toughness, and (c) stress-corrosion-cracking (SCC) resistance at room temperature in Carpenter Custom 465



work. In the present manuscript, the focus will be placed on determining the thermo-mechanical conditions within the weld region which cause these changes

### 3. LFW Process Modeling

#### 3.1 Problem Definition

As mentioned earlier, the main objective of the present work is to develop a process model which can be used to investigate the effect of the LFW process parameters in Carpenter Custom 465 on the spatial distribution and temporal evolution of temperature and material flow in the weld region, as well as the temporal evolution of axial shortening. In our ongoing work, this model is being extended in order to enable prediction of the material microstructural changes in different LFW weld zones.

#### 3.2 Formulation of the Process Model

Modeling of the LFW process carried out in the present work employed a fully coupled thermo-mechanical finite-element procedure, which is an adaptation and extension of the one developed for and applied to the friction stir welding (FSW) process in our prior work (Ref 20-28). The approach used requires specification of the following: (a) computational domain; (b) computational-analysis type; (c) initial conditions; (d) boundary conditions; (e) contact interactions; (f) heat-generation and partitioning; (g) computational algorithm; (h) material thermo-mechanical models; and (i) computational accuracy, stability, and cost. These aspects are briefly over-viewed in the remainder of this sub-section.

#### 3.3 Computational Domain

The computational domain used consists of two (initially) parallelepiped-shaped workpieces with edge dimensions  $L_x$  by  $L_y$  by  $L_z = 20$  mm by 10 by 30 mm. The two workpieces are stacked in the  $z$ -direction so that the initial cross-sectional area of the two faying surfaces is  $L_x$  by  $L_y$  ( $=200$  mm<sup>2</sup>). In accordance with the common LFW practice, reciprocating motion was assumed to take place along the shorter of the two contact-interface directions ( $y$ -direction, in the present case). This is done in order to facilitate flash formation (i.e., expulsion of the plasticized material) and to promote the formation of a good quality weld.

Each of the workpieces is meshed using first-order eight-node hexahedron (cubic or nearly cubic) thermo-mechanically coupled, reduced-integration finite elements. Due to the transient nature of the temperature field and high-temperature sensitivity of the workpiece material properties, mesh size (in the direction normal to the faying surfaces) is chosen in accordance with the steepest temperature gradient (and the stable time increment desired). Due to the highly localized nature of the HAZ and TMAZ, a fine mesh had to be used only in the workpiece region near the contact interface. Typically, each workpiece initially contained ca. 20,000 elements. An example of a typical finite-element mesh used is depicted in Fig. 4 in which, for clarity, only the lower (stationary) workpiece is shown.

#### 3.4 Computational-Analysis Type

The LFW process is analyzed computationally using a fully coupled thermo-mechanical finite-element algorithm, within

which heat dissipation associated with workpiece/workpiece interfacial friction-sliding and plastic deformation is treated as a heat source in the governing heat conduction equation, while the effect of temperature on the mechanical response of the workpiece material is taken into account through the use of temperature-dependent material-model parameters.

#### 3.5 Initial Conditions

The analysis is carried out by prescribing, from the onset, zero values to the stress, and material-particle velocities and the ambient value to the temperature in both workpieces.

#### 3.6 Boundary Conditions

While LFW requires only the relative reciprocating motion of the contacting upper and lower workpieces, for convenience, the lower workpiece is kept stationary in the present work while the reciprocating motion is assigned to the upper workpiece. This is accomplished by assigning zero-displacement boundary conditions (in all three directions) to the bottom face of the lower workpiece. As far as the top face of the upper workpiece is concerned, it is constrained in the  $x$ -direction, subjected to a time-dependent pressure in the  $z$ -direction and assigned a sinusoidal/reciprocating displacement in the  $y$ -direction,  $u_y$ , as

$$u_y = u_0 \sin(2\pi ft), \quad (\text{Eq 1})$$

where  $f$  is the (ordinary) frequency of reciprocating motion (Hz) and  $u_0$  is the reciprocation amplitude.

As far as the thermal boundary conditions are concerned, it is assumed that the temperature at the outer surfaces of the workpieces is controlled by forced convection conditions (induced by the relative reciprocating motion of the workpieces) and by radiation effects. Typical values for the forced convection coefficient of 100 W/m<sup>2</sup>K and for the emissivity of 0.5 were chosen. The same boundary conditions were applied to the portions of the faying surfaces which were exposed (temporarily) as a result of the reciprocating motion of the workpieces.

#### 3.7 Contact Interactions

The workpiece-workpiece normal interactions are analyzed using a penalty-contact algorithm. Within this algorithm, (normal) penetration of the contacting surfaces is resisted by a set of linear springs which produce a contact pressure that is proportional to the depth of penetration. Typically, maximum default values, which still ensure computational stability, are assigned to the (penalty) spring constants. Force equilibrium in a direction collinear with the contact-interface normal then causes the penetration to acquire an equilibrium (contact-pressure-dependent) value. It should be noted that no contact pressures are developed unless (and until) the nodes on the *slave surface* contact/penetrate the *master surface*. On the other hand, the magnitude of the contact pressure that can be developed is unlimited. As far as the tangential workpiece-workpiece interactions (responsible for transmission of the shear stresses across the contact interface) are concerned, they are modeled using a modified Coulomb friction law. Within this law, the maximum value of the shear stresses that can be transmitted (before the contacting surfaces begin to slide) is defined by a product of the contact pressure and a static (before sliding) or a kinetic (during sliding) friction coefficient. In addition, to account for the potential occurrence of a *sticking*



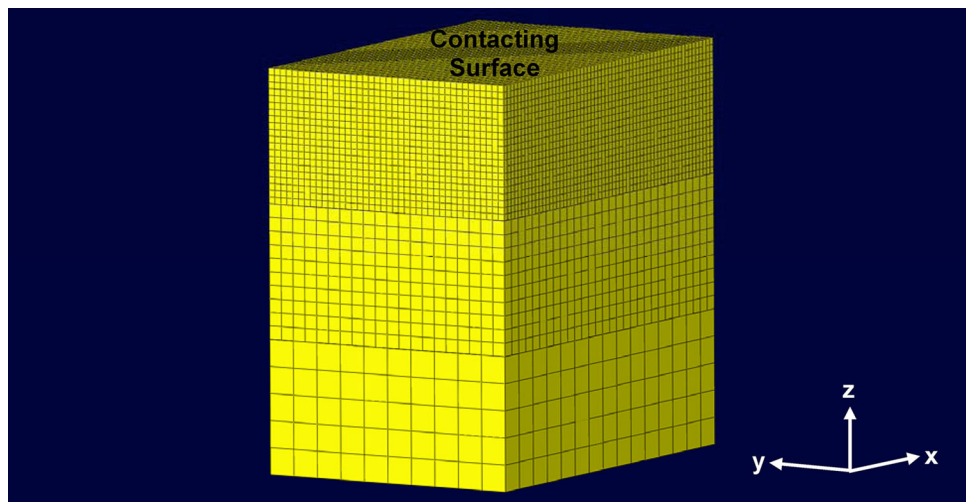


**Fig. 4** Typical finite-element mesh used in the present work. For clarity, only the lower workpiece is shown

*condition* (sliding occurs by shear fracture of the softer workpiece material, in the case of LFW of dissimilar materials, rather than by a relative motion at the contact interface), a maximum value of shear stress (equal to the temperature-dependent shear strength of the softer material) that can be transmitted at any level of the contact pressure, is also specified.

As far as the friction coefficient is concerned, it is generally assumed that in the case of friction-based welding processes, this contact parameter is controlled by the formation and shearing of microwelds (i.e., micron-sized regions at which contacting surface asperities are bonded). Furthermore, it is recognized that the friction coefficient is a function of a number of factors such as the contact interface (mean) temperature, slip speed, contact pressure, faying-surfaces' roughness/topology, etc. Using the experimental and numerical results pertaining to the effect of various contact-interface conditions on the friction coefficient, reported in Ref 29, prototypical functional relations between steel/steel friction coefficient and temperature, slip velocity, and contact pressure are depicted in Fig. 5(a-c), respectively. The functional relations depicted in these figures reflect the effect of the three contact-surface variables on the competition between microweld formation and shear-fracture processes. Specifically, increased temperature and sliding rate lead to material softening, which both increases the tendency for microweld formation and for shear fracture. As far as the effect of contact pressure is concerned, it can promote the development of a local texture within the microwelds and, in turn, a low value of the directionally dependent shear strength.

### 3.8 Heat-Generation and Partitioning

As mentioned earlier, both frictional sliding and plastic deformation act as heat sources during the LFW process. The heat generated by these two phenomena in the workpiece-contact region is subsequently partitioned between the two workpieces.

To account for the heat generated due to frictional sliding, its rate is assumed to scale with the product of local interfacial shear stress and the sliding rate.

As far as work due to plastic deformation is concerned, 95% of this work was assumed to be dissipated in the form of heat,

while the remaining 5% is stored in the form of crystalline defects.

Partitioning of the heat generated during LFW between the two workpieces is computed using the procedure described in Ref 30. According to this procedure, a ratio of the fractions of frictional-sliding-generated heat allotted to the upper and lower workpieces is given by

$$\text{heat-ratio}_{\text{upper/lower}} = \frac{q_{\text{upper}}}{q_{\text{lower}}} = \sqrt{\frac{\lambda_{\text{upper}} \rho_{\text{upper}} c_{p_{\text{upper}}}}{\lambda_{\text{lower}} \rho_{\text{lower}} c_{p_{\text{lower}}}}}, \quad (\text{Eq } 2)$$

where  $\lambda$  is thermal conductivity,  $\rho$  is the mass density, and  $c_p$  is the specific heat of the workpiece material. It should be noted that the  $(q_{\text{upper}} + q_{\text{lower}})$  sum must be equal to the total heat generated during frictional sliding. Examination of Eq (2) reveals that for identical materials of the two workpieces, the heat ratio is equal to unity as expected. Since Eq (2) is frequently used in computational analyses of various frictional-sliding-based welding processes, e.g., LFW, FSW, etc., without providing/explaining the basic foundation of this equation, such an explanation is provided in the remainder of this paragraph. To rationalize Eq (2), the following observations should be made: (a) at any time  $t$ , the distance traveled by the heat front from the contact interface within each of the workpieces scales with  $\sqrt{\alpha}$ , where  $\alpha$  is the respective material thermal diffusivity; (b) for a given instantaneous value of the interfacial temperature, temperature profile integrated over the distance traveled by the heat wave from the interface at a given time also scales with  $\sqrt{\alpha}$ ; and (c) heat absorbed by the workpiece material in the time period  $0$  to  $t$  scales with the product of the material mass density  $\rho$ , its mass-based specific heat  $c_p$ , and the aforementioned integral, i.e., with  $\rho c_p \sqrt{\alpha}$ . Furthermore, since  $\alpha$  is related to thermal conductivity  $\lambda$  as  $\alpha = \lambda / \rho c_p$ , the heat absorbed scales with  $\sqrt{\lambda \rho c_p}$ .

In addition to the heat partitioning between the contacting workpieces, the problem of heat transfer between the workpieces had to be addressed. In the present work, this heat transfer was assumed to be purely conductive. In other words, while in the initial phase of LFW the two workpieces contact only through surface asperities and air-filled pockets exist in the contact region, the contribution of convection and radiation to

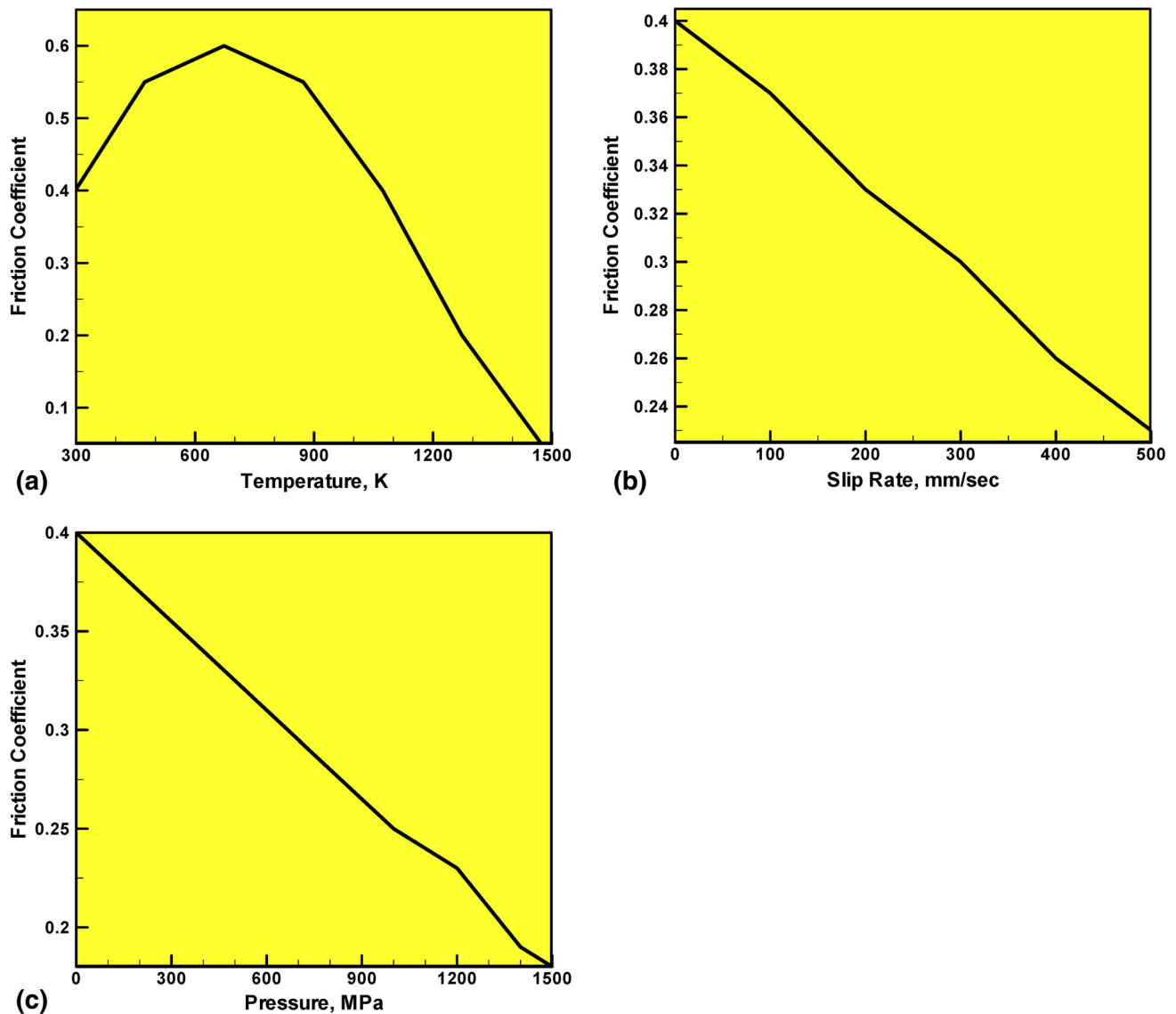


**Fig. 5** Variation of friction coefficient with (a) temperature, (b) slip rate, and (c) contact pressure in prototypical steel/steel sliding contact pairs (Ref 29)

the heat exchange across these pockets was deemed negligible. This was done for the following reasons: (a) in the initial LFW stage, the temperature in the contact region is too low for radiation to play any significant role; and (b) the interfacial pockets are too small and isolated for a convection current to be formed. As far as the conductive heat transfer between the contacting surfaces is concerned, it is defined as the product of the temperature difference between the contacting surfaces and the interfacial thermal conductance. It is well established that the interfacial thermal conductance is a function of the surface topology, contact pressure, and material thermo-mechanical properties (Ref 31). An example of typical ( $T < 500$  K, in air) results pertaining to the effect of contact pressure and mean surface roughness on the stainless-steel/stainless-steel interfacial thermal conductance is depicted in Fig. 6 (Ref 32). Under high-contact pressures and high interfacial temperatures encountered in the course of LFW, plastic deformation of the surface asperities gives rise to high values of the interfacial thermal conductance. Consequently, temperature jumps across

the contact interface are expected to be very small, and are ignored in the present work.

### 3.9 Computational Algorithm

As established earlier, workpiece materials in the weld region experience large plastic deformations during LFW. Under these circumstances, the use of a pure Lagrangian approach in which the finite-element mesh is attached to and moves with the material may be prone to serious numerical problems (due to excessive mesh distortion). To overcome this potential problem, an Arbitrary Lagrangian-Eulerian (ALE) formulation is used within which adaptive re-meshing is carried out of the highly distorted regions of the workpieces to maintain a good quality mesh.

The fully coupled thermo-mechanical ALE problem associated with LFW process modeling is solved numerically using an explicit solution algorithm implemented in ABAQUS/Explicit (Ref 33), a general-purpose finite-element solver. As

will be shown later, a material user-subroutine was developed and linked with this software in order to implement the Carpenter Custom 465 material model (presented in the next section).

### 3.10 Material Thermo-Mechanical Models

For a complete definition of the LFW process model, specification of the thermo-mechanical constitutive models for the subject material(s) is mandatory. Unfortunately, an overview of the public-domain literature did not reveal the existence of such models for Carpenter Custom 465. Consequently, one of the main objectives of the present work was the development of the thermo-mechanical material model for this material. Details of the procedure used and the results obtained are presented in the next section.

### 3.11 Computational Accuracy, Stability and Cost

To keep the computational cost reasonable while ensuring accuracy and stability of the (conditionally stable, explicit) computational procedure, a mass-scaling algorithm is used. This algorithm adaptively adjusts material density in the critical (time-step-controlling) finite elements without significantly affecting the computational-analysis results.

## 4. Material Model Development

In the present analysis, the two workpieces to be welded are assumed to both be made of Carpenter Custom 465, H1000. Consequently, only one thermo-mechanical material model had to be developed in the present work.

### 4.1 Mechanical Model

Following our prior work (Ref 24), the mechanical response of the workpiece material is assumed to be of an elastic/plastic character. The elastic response of the material is assumed to be

isotropic, linear, and temperature dependent, and to be governed by a generalized Hooke's Law. As far as the plastic response of the material is concerned, it is assumed to be strain hardenable, strain rate sensitive, and thermally softenable, and to be described by the Johnson-Cook material model (Ref 34). Plastic anisotropy, as quantified by the Lankford coefficient  $R$ , is neglected since in Carpenter Custom 465, H1000,  $R$  takes on values near 1.0 (Ref 19).

The room-temperature Young's modulus of Carpenter Custom 465, H1000, has been reported in Ref 19 as 199 GPa. On the other hand, no public-domain data pertaining to the effect of temperature on the Young's modulus of this material could be identified. To overcome this lack of data, a computational procedure is adopted within which it is assumed that temperature dependence of the Young's modulus in Carpenter Custom 465, H1000, is identical, on a relative basis, to that of another related stainless steel. Examination of the public-domain literature identifies temperature dependence of the Young's modulus of 440C martensitic stainless steel in

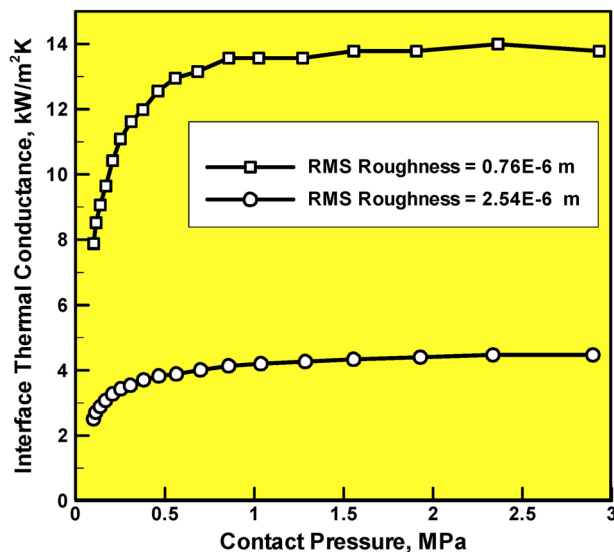


**Fig. 6** The effect of contact pressure and surface roughness on stainless-steel/stainless-steel interfacial thermal conductance in air (Ref 32)

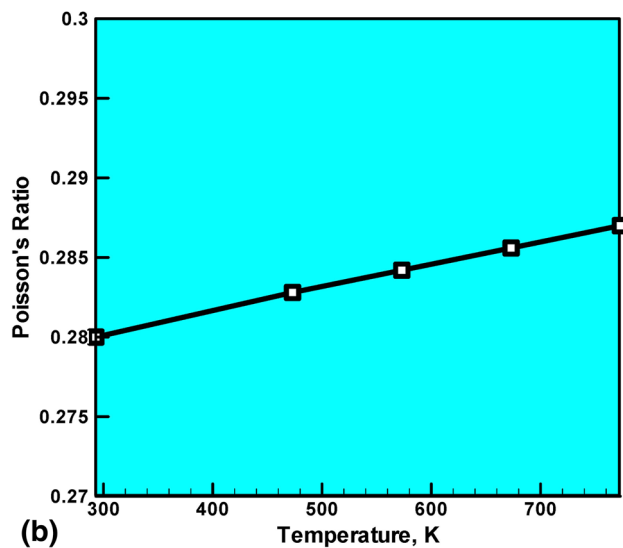
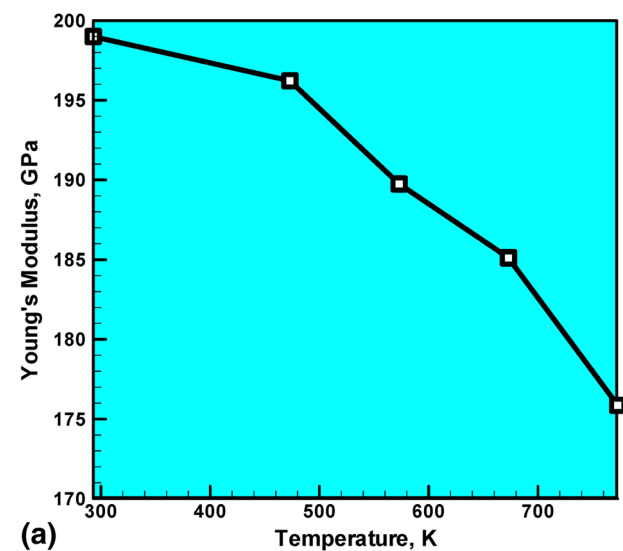


**Fig. 7** Temperature dependence of (a) the Young's modulus and (b) the Poisson's ratio in Carpenter Custom 465, H1000, derived using a property correlation analysis and experimental data reported in Ref 35

Ref 35 as the best source of data for inferring temperature dependence of Carpenter Custom 465, H1000. The aforementioned procedure yielded temperature dependence of the Young's modulus of Carpenter Custom 465, H1000, as depicted in Fig. 7(a). Following the same procedure and the same source reference, temperature dependence of the Poisson's ratio in Carpenter Custom 465, H1000, has been determined, Fig. 7(b).

As mentioned earlier, plastic behavior of the workpiece material during LFW is represented using the Johnson-Cook model (Ref 34). This model is capable of accounting for the material behavior under large-strain, high-deformation rate, and high-temperature conditions, the type of conditions commonly encountered in the problem of computational modeling of the LFW process. Within the Johnson-Cook material model, the workpiece material yield strength is assumed to be controlled by strain- and strain-rate hardening, as well as by reversible thermally activated slip-controlled thermal-softening effects, and is given by the following functional relation:

$$\sigma_y = [A + B(\bar{\epsilon}^{pl})^n] [1 + C_1 \ln(\dot{\bar{\epsilon}}^{pl} / \dot{\bar{\epsilon}}_0^{pl})] [1 - T_H^m], \quad (\text{Eq 3})$$

where  $\sigma_y$  is the yield strength;  $\bar{\epsilon}^{pl}$  is the equivalent plastic strain;  $\dot{\bar{\epsilon}}^{pl}$  is the equivalent plastic strain rate;  $\dot{\bar{\epsilon}}_0^{pl}$  is a reference equivalent plastic strain rate;  $A$  is the zero-plastic-strain, unit-plastic strain rate, room-temperature yield strength;  $B$  is the strain-hardening constant;  $n$  is the strain-hardening exponent;  $C_1$  is the strain rate constant;  $m$  is the thermal-softening exponent; and  $T_H = (T - T_{\text{room}}) / (T_{\text{melt}} - T_{\text{room}})$  a room-temperature ( $T_{\text{room}}$ ) based homologous temperature while  $T_{\text{melt}}$  is the melting temperature. All temperatures are given in Kelvin.

As stated earlier, there are no public-domain data pertaining to the strain-/strain-rate hardening and thermal softening of Carpenter Custom 465, H1000. In other words, parameterization of the Johnson-Cook material model is not available and could not be constructed based on the available experimental data. To overcome this lack of data, a material-property correlation analysis is developed and applied. Within this analysis, it is assumed that (a) the Johnson-Cook material-model parameters are related to the basic material properties such as the stacking fault energy, the number of independent slip systems, the character of the dominant strengthening mechanism (e.g., precipitation-hardening, strain-hardening, and solution-strengthening), etc.; and (b) available Johnson-Cook material-model parameters for a related material can be used to assess the required parameters for Carpenter Custom 465, H1000. Specifically, to parameterize the Johnson-Cook material model for Carpenter Custom 465, H1000, the following steps were taken:

- The ascending portion of the room-temperature uniaxial engineering-stress/strain curve obtained under a nominal plastic strain rate of  $0.01 \text{ s}^{-1}$  (Ref 36), Fig. 8, is first fitted to a function  $\sigma_y = [A + B(\bar{\epsilon}^{pl})^n]$ , using a non-linear regression analysis. This procedure yielded the following Johnson-Cook material-model parameters:  $A = 1470 \text{ MPa}$ ,  $B = 1575 \text{ MPa}$ ,  $n = 0.53$ , and  $\dot{\bar{\epsilon}}_0^{pl} = 0.01 \text{ s}^{-1}$ ;
- The strain-rate hardening parameter,  $C$ , is determined using the following steps:
  - by differentiating yield stress as defined by Eq (3), in which the strain-hardening and thermal-softening terms are omitted, with respect to the natural logarithm of the plastic strain rate, it is found that

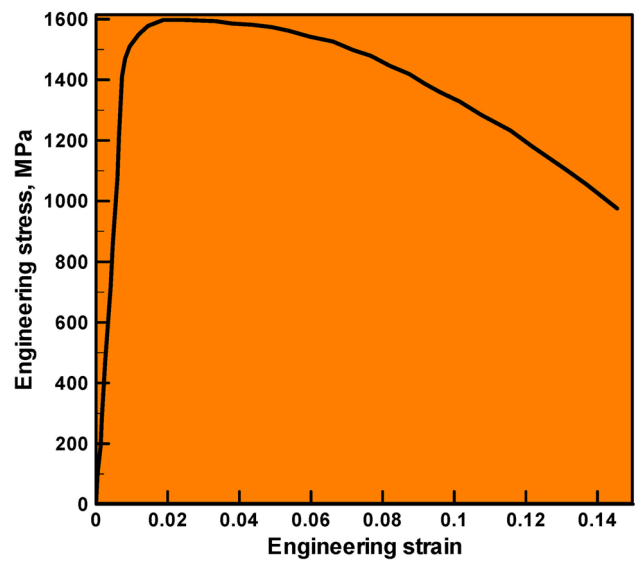


**Fig. 8** The room temperature uniaxial engineering-stress/strain curve for Carpenter Custom 465, H1000, obtained under a nominal plastic strain rate of  $0.01 \text{ s}^{-1}$  (Ref 36)

$$C = \frac{1}{A} \frac{\partial \sigma_y}{\partial (\ln \dot{\bar{\epsilon}}^{pl})}. \quad (\text{Eq 4})$$

- The second term on the right-hand side of Eq (4) is next expressed using the conventional thermally activated deformation theory in which the rate of plastic deformation is defined by the following Arrhenius-type equation:

$$\dot{\bar{\epsilon}}^{pl} = \dot{\bar{\epsilon}}_a^{pl} \exp\left(\frac{-\Delta G}{RT}\right), \quad (\text{Eq 5})$$

where  $\dot{\bar{\epsilon}}_a^{pl}$  is an equivalent plastic strain-rate parameter (which scales with the attempt frequency of dislocations to overcome the rate-controlling obstacles to slip-based deformation),  $\Delta G$  is the associated activation energy, and  $R$  is the universal gas constant. Within the theory of thermally activated slip, e.g., (Ref 37), the activation energy  $\Delta G$  is defined by the following expression:

$$\Delta G = \Delta G_0 \left[1 - \left(\frac{\sigma_y}{s}\right)^p\right]^q, \quad (\text{Eq 6})$$

where  $\Delta G_0$  is the maximum activation energy associated with dislocation motion in the absence of any applied stress,  $s$  is the material yield strength in the absence of thermal activation, and  $p, q$  are obstacle-shape defining parameters. Parameters  $\Delta G_0, p$ , and  $q$  are characteristics of (and their values are governed by the slip-controlling) dislocation-obstacle interactions.

By combining Eq (5) and (6) and rearranging, the following expression is obtained:

$$\sigma_y = s \left[1 - \left(\frac{RT}{-\Delta G_0} \ln\left(\frac{\dot{\bar{\epsilon}}^{pl}}{\dot{\bar{\epsilon}}_a^{pl}}\right)\right)^{\frac{1}{q}}\right]^{\frac{1}{p}}. \quad (\text{Eq 7})$$

After differentiating Eq (7) to obtain  $\partial \sigma_y / \partial (\ln \dot{\bar{\epsilon}}^{pl})$  (the resulting expression is too cumbersome to be shown), the resulting equation is evaluated at  $T = 300 \text{ K}$  and  $\dot{\bar{\epsilon}}^{pl} = 0.01 \text{ s}^{-1}$ . During this evaluation, it is assumed that



due to attendant high dislocation density in lath martensite of Carpenter Custom 465, H1000, interaction of glide dislocations with (repulsive) forest dislocations is the deformation-mechanism-controlling material strength. Consequently, typical values for this type of dislocation/obstacle interactions are assigned to the five obstacle-characterizing parameters, i.e.,  $\Delta G_0 = 400$  kJ/mol,  $s = 2500$  MPa,  $\dot{\epsilon}_a^{pl} = 10 \text{ s}^{-1}$ ,  $p = 2/3$ , and  $q = 2$ . The resulting value for  $\partial \sigma_y / \partial (\ln \dot{\epsilon}^{pl})$  is used in Eq (4) to obtain  $C = 0.0347$ .

- (c) According to the Johnson-Cook material model, thermal softening is governed by two material parameters,  $T_{\text{melt}}$  and  $m$ . The  $T_{\text{melt}} = 1673$  K for Carpenter Custom 465, H1000, has been reported in Ref 19. Parameter  $m$  is not generally assigned a physical meaning and is treated mainly as a fitting parameter. However, it is generally found that in materials with comparable chemistries and microstructures, this parameter takes on similar values. Adopting this observation,  $m$  parameter for Carpenter Custom 465, H1000, has been set to a value ( $m = 1.75$ ) equal to an average of values for several precipitation-hardened martensitic steels (Ref 36).

For convenience, a summary of the general, room-temperature linear elasticity, and Johnson-Cook material-model parameters for Carpenter Custom 465, H1000, determined in the present work, is provided in Table 1.

It should be noted that in the original Johnson-Cook material model, temperature affects the material strength only reversibly by promoting thermal activation of dislocation motion. In other words, no permanent changes in the room-temperature material microstructure and properties are assumed to result from a high-temperature exposure of the material. This assumption is not fully justified in the case of LFW, where it is commonly observed that high temperatures in the weld give rise to dynamic recovery/recrystallization with the accompanying sub-grain formation and grain-size refinement. In addition, in age-hardened materials such as Carpenter Custom 465, exposure of the material to high temperatures may lead to over-aging, precipitate dissolution, and austenite reversion. Following the approach proposed in Ref 16, potential modifications to the Johnson-Cook material model are being investigated in our ongoing work. Specifically, parameter  $A$  in Eq (3) is being considered not as a constant, but rather as an instantaneous-microstructure-dependent quantity.

While the original Johnson-Cook material model is available as a built-in model within ABAQUS/Explicit (Ref 33) and the

user is only required to provide values of the parameters  $A$ ,  $B$ ,  $n$ ,  $C$ ,  $\dot{\epsilon}_0^{pl}$ ,  $T_{\text{melt}}$ ,  $T_{\text{room}}$ , and  $m$ , this model is implemented in a user-material subroutine (VUMAT) and linked with the ABAQUS/Explicit solver. This was done in order to initiate development and implementation of the aforementioned modifications to the Johnson-Cook material model. Full implementation of these modifications will be presented in our future work. To validate the current implementation of the Johnson-Cook material model, several LFW cases were analyzed using both the user-material model and the built-in Johnson-Cook material model (with the same parameterizations). The corresponding results (not shown for brevity) are found to be practically identical, validating the current implementation of the Johnson-Cook material model.

## 4.2 Thermal/Thermo-Elastic Model

As far as the thermal response of Carpenter Custom 465 is concerned, it is assumed to be isotropic and temperature dependent. The thermal model used includes two material parameters: (a) thermal conductivity,  $k$ ; and (b) specific heat,  $c_p$ . Temperature dependencies of these parameters (Ref 19, 37) are depicted in Fig. 9(a) and (b). In addition, the temperature dependencies of the true and room-temperature-based mean values of the linear thermal expansion coefficient, a thermo-elastic parameter which controls the extent of thermal strains, for the same material are shown in Fig. 9(c) and (d) (Ref 19).

## 4.3 Validation of the Material Model

To validate the thermo-mechanical material model for Carpenter Custom 465, H1000 developed in the present work, simulations of a high-temperature ring-compression test are carried out, and the results obtained were compared with their experimental counterparts (generated in our ongoing experimental investigation). Within the ring-compression test, a ring-shaped test sample is compressed between two flat platens. During compression, the outer diameter of the specimen increases. On the other hand, depending on the magnitude of the friction coefficient, the inner diameter may either decrease (in the case of a relatively large friction coefficient) or increase (in the case of a relatively small friction coefficient). Thus, the comparison of the simulated and experimental ring-compression results does not only help validate the thermo-mechanical material model but also the contact model developed in Section III.

The ring-shaped test specimen had the following dimensions: inner diameter = 6 mm, outer diameter = 11 mm, and height = 6 mm. In order to replicate the contact conditions encountered in the LFW process simulations, both the test specimen and the platens are made of Carpenter Custom 465, H1000. The results presented and discussed in this section were obtained at a test temperature of 973 K, and at a test-machine cross-head velocity of 0.2 mm/s.

In Fig. 10(a) and (b), a comparison is provided between the computed and experimental results pertaining to the evolution of the inner and outer diameters, respectively, of the ring-shaped specimen in the course of compression. It is seen that the agreement between the computed and experimental results is fairly good.

In Fig. 10(c), a comparison is given between the computed and experimental results pertaining to the load vs. specimen-height reduction relationship in the course of compression. Again, the agreement between the two sets of results is reasonable.

**Table 1 General, room-temperature linear elasticity, and Johnson-Cook plasticity material-model parameters for Carpenter Custom 465**

Parameter	Symbol	Units	Value
Density	$\rho$	kg/m <sup>3</sup>	7840
Young's Modulus	$E$	GPa	199.0
Poisson's ratio	$\nu$	N/A	0.28
Reference strength	$A$	MPa	792.0
Strain-hardening parameter	$B$	MPa	510.0
Strain-hardening exponent	$n$	N/A	0.26
Strain-rate coefficient	$C$	N/A	0.014
Room temperature	$T_{\text{room}}$	K	293
Melting temperature	$T_{\text{melt}}$	K	1673.0
Temperature exponent	$m$	N/A	1.03

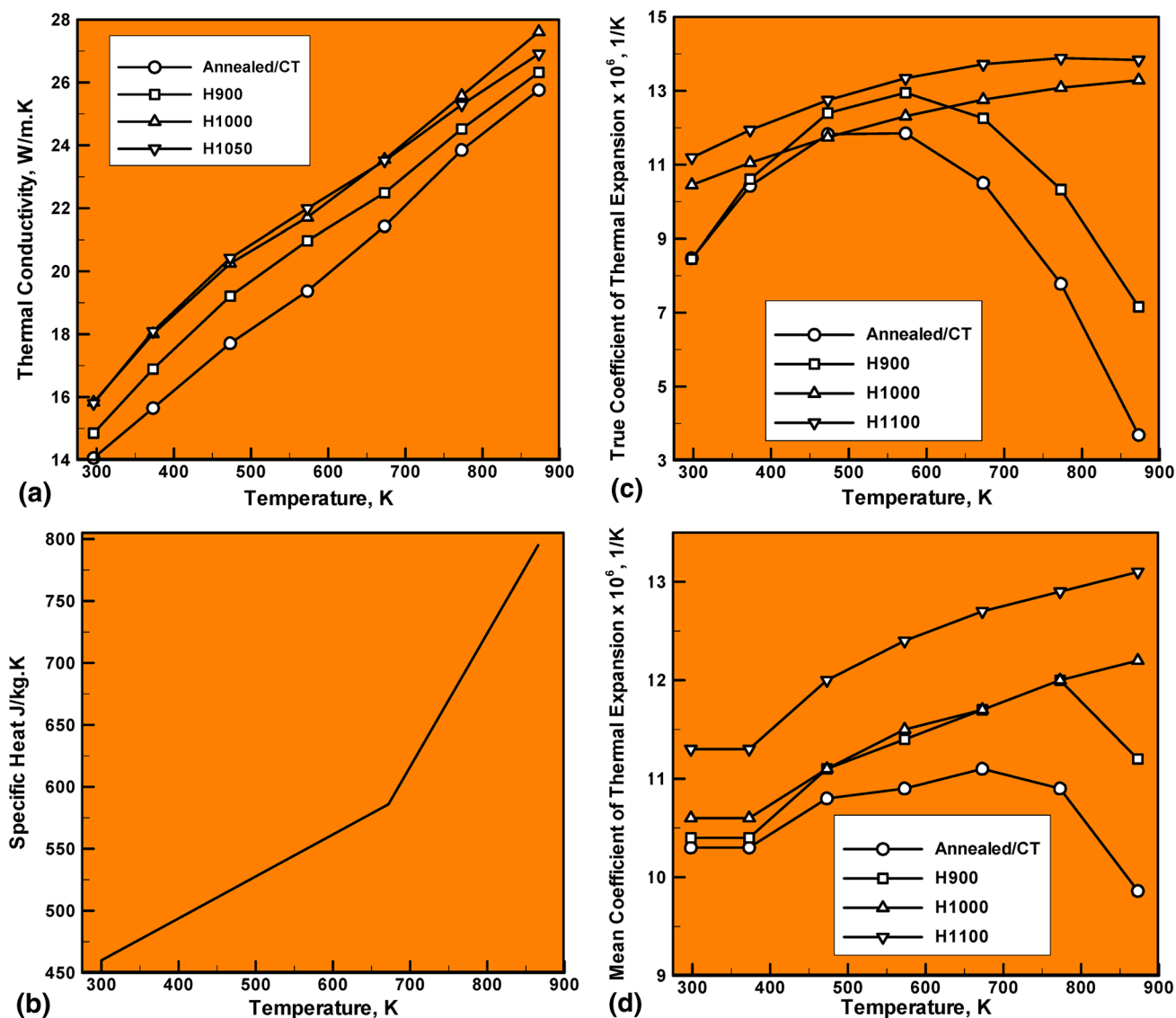


**Fig. 9** Variation of (a) thermal conductivity, (b) specific heat, (c) true linear thermal expansion coefficient, and (d) room-temperature-based mean thermal expansion coefficient with temperature in Carpenter Custom 465 with different heat-treated conditions (Ref 19, 34). Please see text for explanation of the line labels

In Fig. 10(d), a comparison is given between the computed and experimental results pertaining to the temperature evolution at a point initially located as follows: (a) vertical position—half the specimen height, and (b) radial position—the average of the inner and outer diameters. Again, the agreement between the two sets of results is acceptable.

Based on the findings reported in this section, it appears that the newly developed thermo-mechanical material model for Carpenter Custom 465, H1000, as well as the contact model provide reasonable predictions of the Carpenter Custom 465, H1000, mechanical behavior under high-temperature and high-contact-pressure loading conditions.

## 5. Results and Discussion

In this section, a few results pertaining to the application of the newly developed LFW process model to Carpenter Custom

465, H1000 (represented by the newly developed thermo-mechanical material model), are presented and discussed. These results pertain to the spatial distribution and temporal evolution of the temperature and deformation fields (the fields which affect microstructure evolution and spatial distribution within the weld regions). While the prediction of the microstructural changes within the weld is the subject of our ongoing investigation, an example of the results pertaining to the weld microstructure will also be presented.

Specifically, the results presented and discussed in this section pertain to the effect of the LFW process parameters in Carpenter Custom 465, H1000, on (a) spatial distribution and temporal evolution of the interface temperature, (b) temporal evolution and geometry of the expelled material/flash, (c) temporal evolution of the axial shortening, and (d) as-welded microstructure prediction. The LFW process parameters considered here include (a) contact-pressure history throughout different phases of the LFW process, (b) reciprocation frequency, (c) reciprocation amplitude, and (d) number of



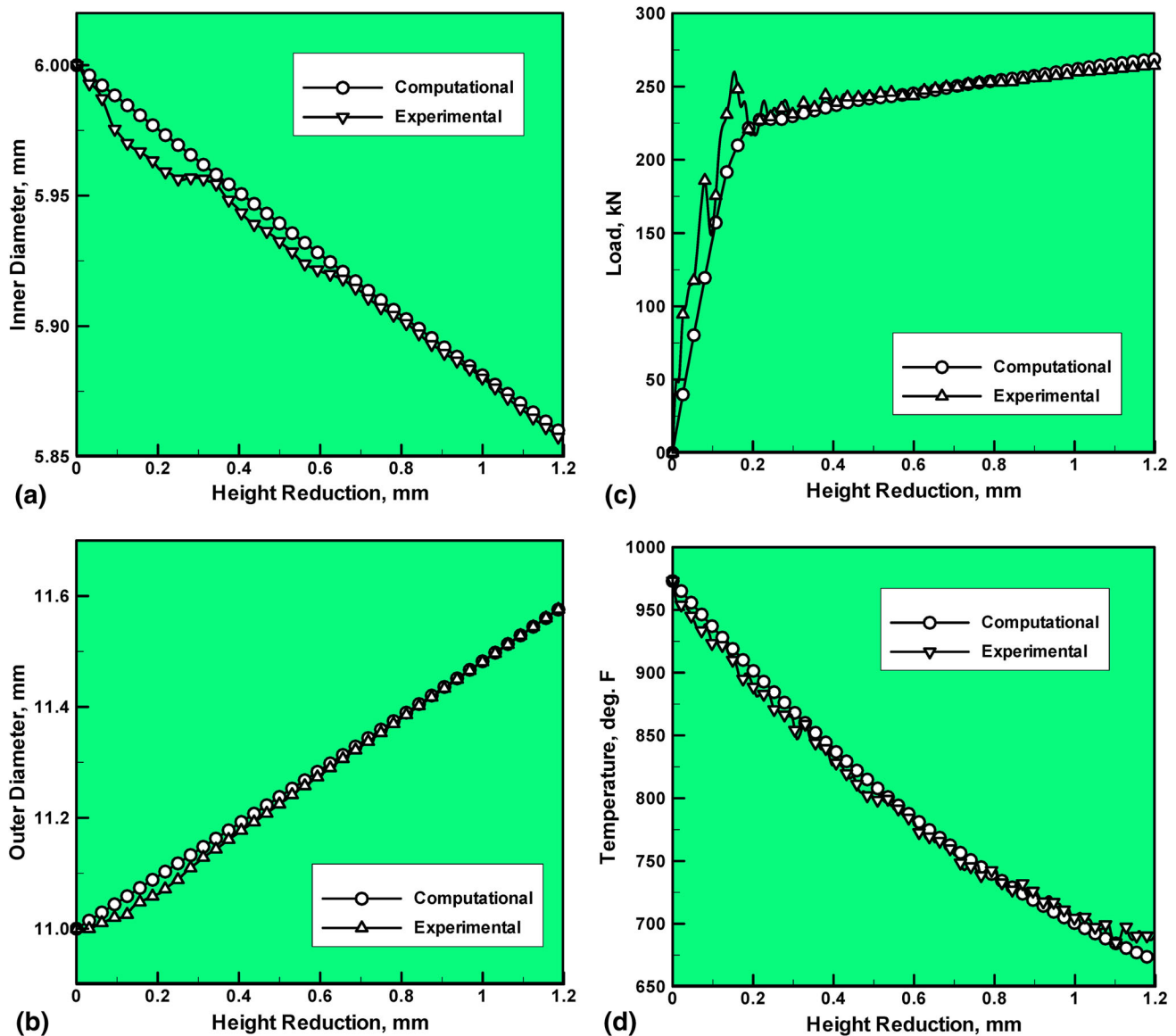


**Fig. 10** Comparison between computed and experimental results pertaining to the evolution, during 973 K ring-compression, of (a) inner diameter, (b) outer diameter, (c) load vs. specimen-height reduction relationship, and (d) temperature at a point initially located at half the specimen height and at the average of the inner and outer diameters

reciprocation cycles or total duration of reciprocating motion. A schematic is provided in Fig. 11(a) and (b) in order to help clarify the definition and time history of the LFW process parameters. An example of the test matrix used in the present work showing the levels of the reciprocation amplitude, reciprocation frequency, and contact pressure in the first three LFW phases is displayed in Table 2.

### 5.1 Spatial Distribution and Temporal Evolution of the Interface Temperature

From the standpoint of obtaining a sound weld with good mechanical properties, temperature uniformity over the contact interface, as well as the maximum value of the interface temperature, attained during the course of the LFW process is of major concern. This was the main reason that temperature uniformity and maximum interface temperature, during LFW, are recorded and analyzed in the present work.

An example of typical results pertaining to the temperature (in K) distribution over the contact interface within the LFW equilibrium phase is displayed in Fig. 12(a). The results displayed in this figure show that the temperature difference between the central region of the contact interface and the interface edges is ca. 35 K. The main reason for the observed non-uniformity in the temperature distribution along the contact interface is the periodic loss of contact between the faying surfaces over edge regions which extend orthogonally to the direction of reciprocation and whose widths are equal to the reciprocating amplitude. In these regions of the contact interface, temperatures are lower for two main reasons: (a) heat is not being generated; and (b) heat is being lost via convection and radiation, while these regions are being exposed, i.e., not in contact.

Depending on the choice of the LFW process parameters (reported in Table 2), the maximum temperature difference over the contact interface was found to range between 30 and

180 K. Clearly, for improved quality of the LFW joint, LFW process parameters should be selected in such a way that this temperature difference is minimized. The LFW process simulation parametric study carried out in the present work clearly demonstrated that this can be achieved through (a) reduced reciprocation amplitude, (b) increased reciprocation frequency, and (c) increased levels of the contact pressure. This is depicted graphically in Fig. 13, which shows, at a constant level of the reciprocation amplitude (=2 mm), the effect of contact pressure and the reciprocation frequency on the maximum temperature difference over the contact interface during the LFW equilibrium phase. Due to the aforementioned difficulties associated with the measurements of interfacial temperature and its temporal evolution and spatial distribution, the results pre-

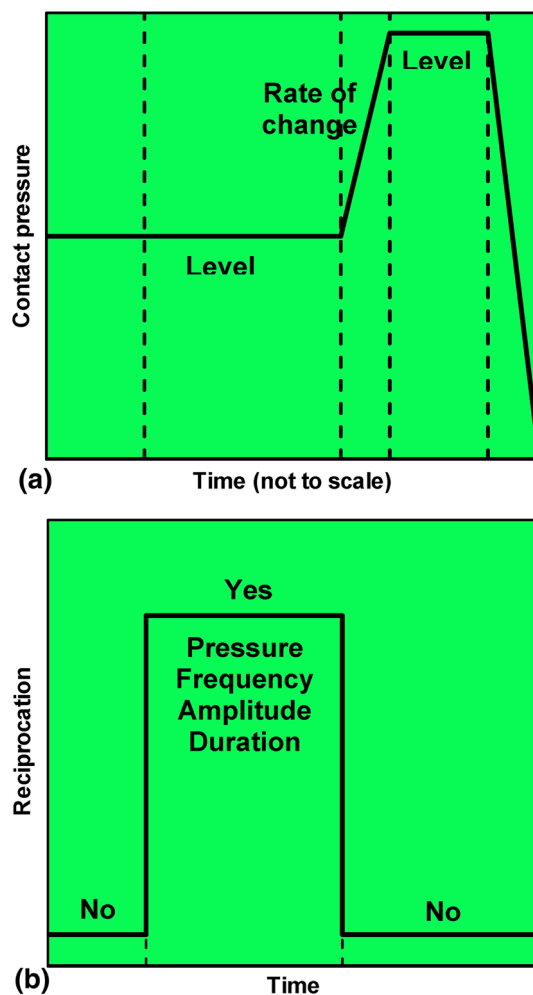


**Fig. 11** Schematic variations of (a) the contact pressure and (b) the reciprocating motion parameters throughout different LFW phases

sented in Fig. 12(a) and (b) and 13 cannot be validated directly. An indirect validation of these results was obtained in our ongoing experimental investigation, which showed that the temperature uniformity over the contact interface results in microstructural uniformity over this interface.

The second aspect of the interface temperature is its maximum value attained during the LFW process. Clearly, this maximum temperature must not exceed the material's solidus temperature. However, attainment of this condition may still yield undesirable results regarding the mechanical properties of the weld if the maximum interface temperature exceeds the temperature ( $A_S$ ) for the onset of martensite  $\rightarrow$  austenite transformation (estimated as 1045 K for Carpenter Custom 465, H1000). An example of the typical results pertaining to temporal evolution of temperature at the center of the contact interface is shown in Fig. 12(b). It is seen that, during the transition phase, temperature steeply rises and that, during the equilibrium phase, temperature oscillates over a relatively narrow range. Furthermore, examination of Fig. 12(b) suggests that there is a possibility for formation of austenite at this location (the location which experiences the highest temperatures in the course of LFW), since the maximum temperature (ca. 1100 K) exceeds the  $A_S$  temperature. The aforementioned parametric study revealed that the maximum temperature experienced by the center of the contact interface can be made lower than  $A_S$  by proper selection of the LFW process parameters. In addition, one must take into account the fact that the material residing at the contact interface, i.e., the material that is subjected to the highest temperatures, is continuously expelled outward to form flash. Thus, formation of austenite appears to be less of a concern during the LFW process. Furthermore, due to a continuous expulsion of the material from the contact surfaces, material over-aging within the weld during the LFW process appears to be of less concern. These findings have been confirmed in our ongoing weld-microstructure characterization experimental investigation, which confirmed the absence of melting, austenite, and excessive over-aging in the weld region.

## 5.2 Temporal Evolution and Geometry of the Expelled Material/Flash

As explained earlier, LFW is accompanied by the formation of flash. Flash contains the material which was previously located at the contact surfaces and was, in the course of LFW, heated, softened, and subsequently expelled in the direction of reciprocation. Formation of the flash during LFW is highly critical since the expelled material was, before expulsion, typically oxidized, contaminated, or otherwise compromised and its removal creates clean, virgin-material surfaces with high affinity for adhesion/bonding.

An example of the typical results pertaining to the temporal evolution of flash during the equilibrium phase of LFW of

**Table 2** An example of the Carpenter Custom 465, H1000, LFW process parameter test matrix used in the present work

Parameter, units	LFW phase			
	Initial	Transition	Equilibrium	Deceleration
Reciprocation amplitude, mm	0.0	0.5, 1.0, 1.5, 2.0		0.0
Reciprocation frequency, Hz	0	25, 35, 45, 55	0	
Contact pressure, MPa	200, 400, 600			600, 800

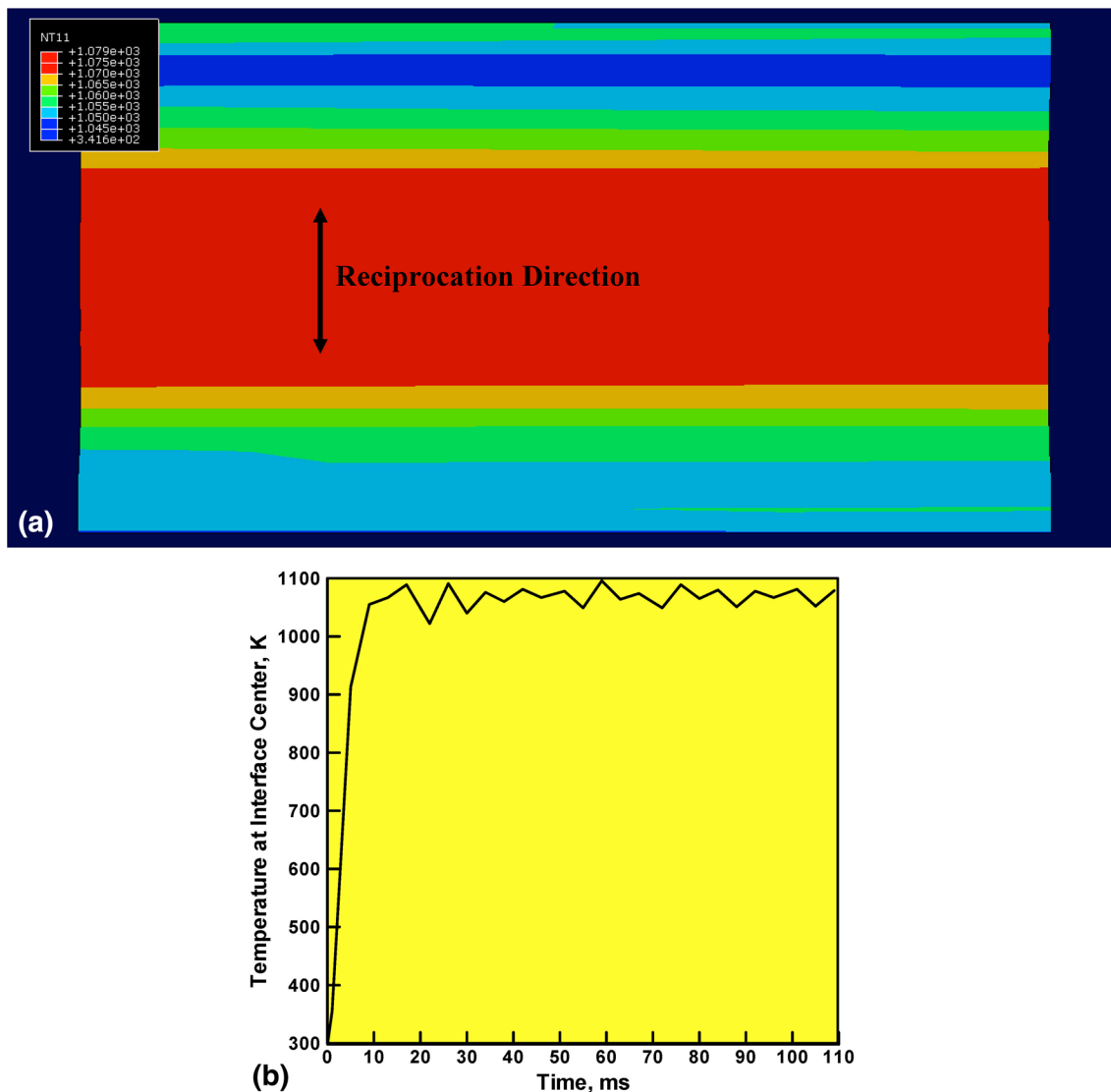


**Fig. 12** Examples of the typical temperature-based results obtained during LFW process simulation of Carpenter Custom 465, H1000, (a) typical temperature (in K) distribution over the contact interface and (b) temporal evolution of temperature at the contact-interface center point

Carpenter Custom 465, H1000, is displayed in Fig. 14(a) and (d). It should be noted that a surface temperature contour plot is superimposed onto the material distribution plot in this figure in order to help relate the local temperature with the extent/rate of flash formation. Examination of the results displayed in Fig. 14(a) and (d) show that a single flash (on each weldment side) is formed, suggesting a good quality weld. This finding was confirmed in our ongoing experimental investigation.

### 5.3 Temporal Evolution of the Axial Shortening

As the thermally softened interface material is expelled, the height/thickness of the two workpieces being welded is reduced. This phenomenon is commonly referred to as *axial shortening*. It is generally accepted that a minimum value of axial shortening (which ensures complete removal of the oxidized, contaminated or otherwise compromised material from the contact surfaces) is necessary for the attainment of a sound weld with good mechanical properties. It is equally well recognized that excessive axial shortening leads to a loss of

material and productivity, as well as to an increased cost associated with removal and handling of excessive flash.

An example of typical results pertaining to the temporal evolution of axial shortening during LFW of Carpenter Custom 465, H1000, is displayed in Fig. 15(a). For improved clarity, different LFW phases are denoted in this figure. It is seen that shortening begins in the initial phase (due to application of the contact pressure) and, after a short transition phase, continues throughout the equilibrium phase at a fairly constant average rate. In the forging phase, application of a higher upset contact pressure causes an abrupt jump in the axial shortening.

The average slope of the axial-shortening vs. time curve in the LFW equilibrium phase defines the rate of axial shortening, also sometimes referred to as the *burn-off rate*. This quantity plays an important role in the LFW process, since it is generally believed that its value must exceed a minimum critical level for the attainment of a sound weld. The rate of axial shortening is a function of the LFW process parameters. This is demonstrated in Fig. 15(b) in which, at a constant level of reciprocation amplitude of 2 mm, a contour plot is displayed showing the effect of the (friction) contact pressure and the reciprocation

frequency on the equilibrium-phase axial-shortening rate. Examination of the results displayed in these figures reveals that, as expected, both increases in the friction contact pressure and reciprocation frequency lead to increases in the axial-shortening rate. The axial-shortening and burn-off results presented in this section could not be currently validated. In our ongoing experimental investigation, efforts are underway to develop axial-shortening/burn-off rate measuring capabilities.

#### 5.4 As-Welded Microstructure Prediction

As demonstrated in the previous section, the LFW process model enables the prediction of the effect of various process

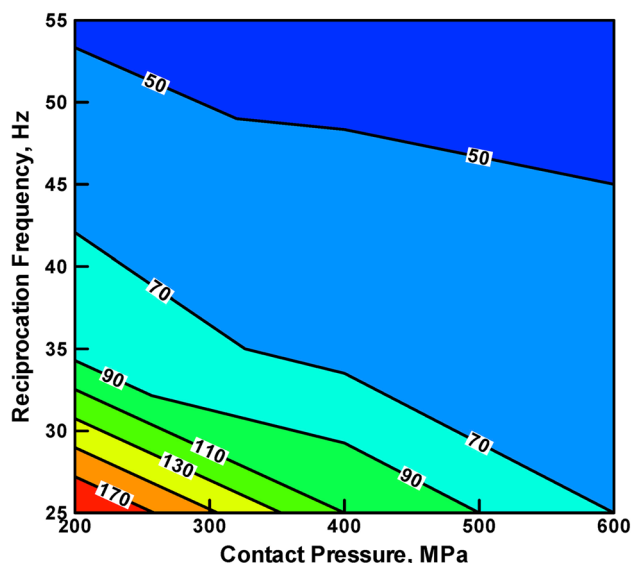


**Fig. 13** The effect of the contact pressure and reciprocation frequency on the maximum temperature difference (in K) along the contact interface of LFW of Carpenter Custom 465, H1000, at a constant level of the reciprocation amplitude of 2 mm

parameters on the temporal evolution and spatial distribution of temperature and material flow fields, as well as the time history of axial-shortening/burn-off rate. In our ongoing investigation, the current work is extended in two directions: (a) a module is being added to the LFW process model in order to enable prediction of the material-microstructure evolution within the weld, and (b) a companion experimental investigation of the LFW process and the weld-microstructure characterization are being developed. These extensions of the present work will enable full validation of the newly developed LFW process model. In the remainder of this section, an example of the results, being generated in our ongoing investigation, which are used for the LFW process model validation is presented and discussed.

In Fig. 16(a) and (b), a comparison is provided of the experimental and computational results pertaining to the spatial distribution of the precipitate mean radius (in microns) over the mid-plane/contact surface of the LFW joint. The results presented in Fig. 16(a) are obtained using standard microstructure-characterization (i.e., optical and scanning electron microscopy) techniques. The results presented in Fig. 16(b) are obtained using the microstructure-evolution module mentioned above. This module enables determination of the type, the extent, and the temporal evolution and spatial distribution of microstructural changes within different portions of the weld [38–41]. The module is based on the key physical metallurgy concepts and principles of Carpenter Custom 465, H1000, and includes the basic thermodynamics and kinetics of various interacting and competing phase transformations which may take place within the weld region of this material. For example, the multi-component nature of the material is accounted for, as well as the kinetics of precipitate nucleation, growth and coarsening over an arbitrary local thermal history (the history yielded by the LFW process model).

It should be noted that material residing within the flash is not accounted for in Fig. 16(a) and (b), for the following two reasons: (a) this material does not ultimately reside within the weldment and, hence, its precipitate microstructure is of no

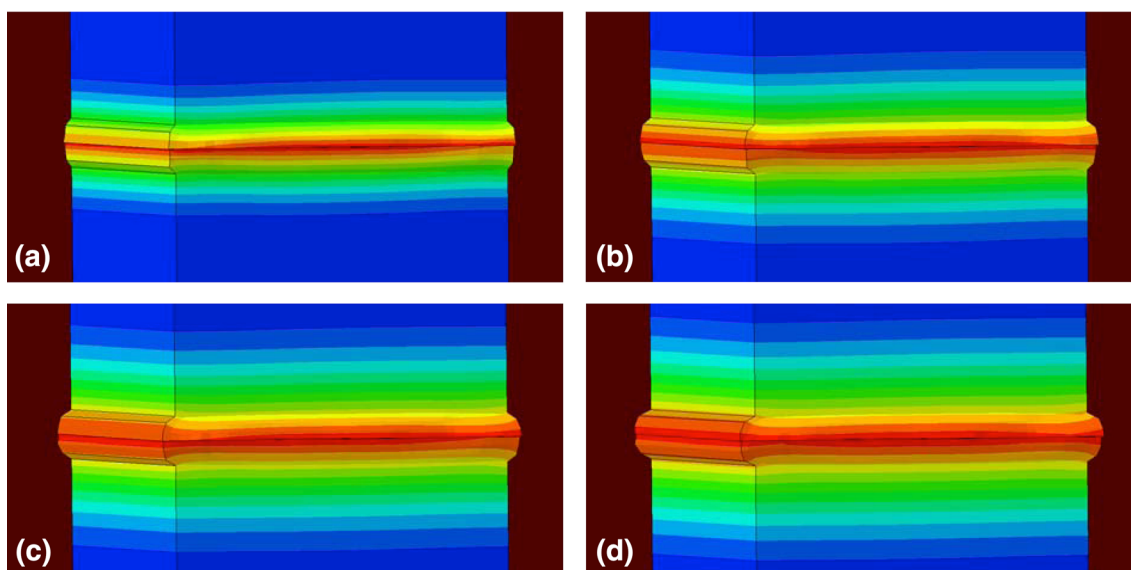


**Fig. 14** Typical results pertaining to the temporal evolution of flash during equilibrium phase of LFW of Carpenter Custom 465, H1000, obtained in the present work. Elapsed time between two consecutive field plots is 0.12 s. Please note that a surface temperature contour plot is superimposed onto the material distribution plot in order to help relate the local temperature to the extent/rate of flash formation

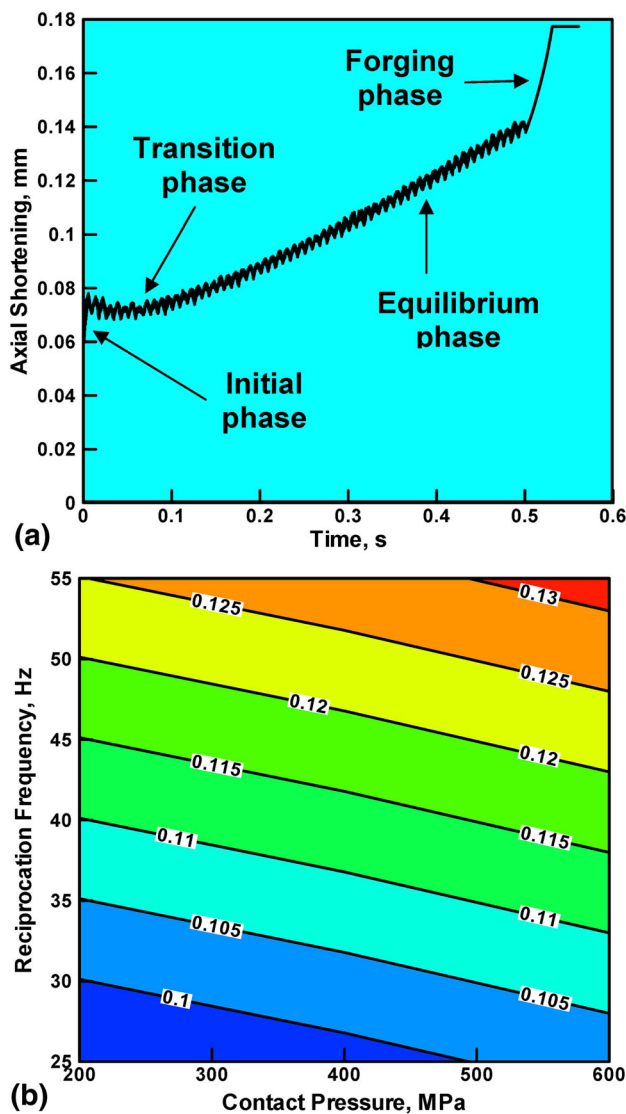


**Fig. 15** Typical results pertaining to (a) temporal evolution of axial shortening and (b) the effect of the equilibrium-phase contact pressure and reciprocation frequency, at a constant level of the reciprocation amplitude of 2 mm, on the rate of axial shortening, both for Carpenter Custom 465, H1000

concern; and (b) the material residing within the flash typically is subjected to excessive temperatures which may result in martensite-to-austenite reversion, the phase transformation which was not accounted for in the microstructure-evolution module.

A comparison of the results displayed in Fig. 16(a) and (b) reveals that (a) the precipitate size is generally non-uniform over the contact interface. Specifically, the largest precipitate sizes are found in the innermost portion of the corresponding x-y section, the portion which experiences the highest temperature. The edge portions of this section contain smaller particle sizes due to the operation of heat-transfer processes between the workpieces being welded and the surroundings, (b) the experimental and computed results pertaining to the spatial distribution of the precipitate mean radius over the faying surfaces are in decent agreement, and (c) the overall size of the precipitates is fairly well accounted for by the microstructure-evolution module.

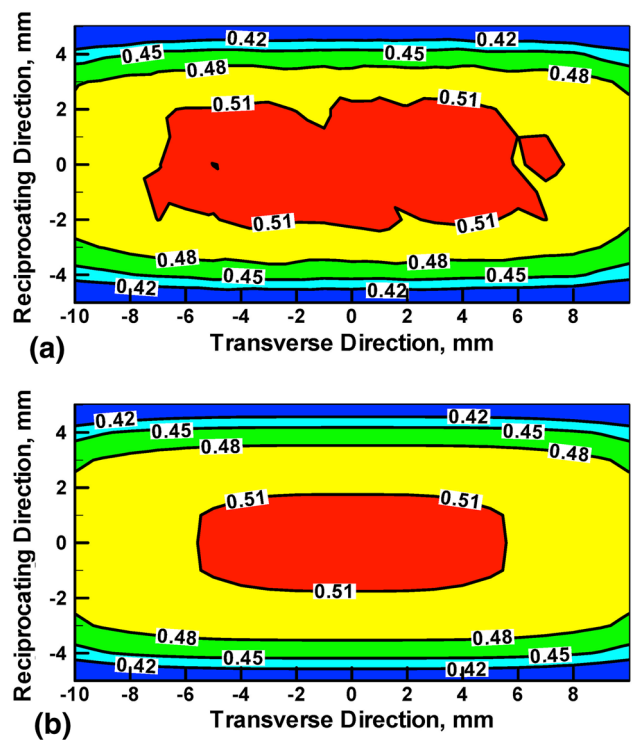


**Fig. 16** Comparison of (a) experimental and (b) computational results pertaining to the spatial distribution of the precipitate mean radius (in microns) over the mid-plane/contact surface of the LFW joint in Carpenter Custom 465, H1000

## 6. Summary and Conclusions

Based on the work presented and discussed in the present paper, the following main summary remarks and conclusions can be made:

1. A LFW process model for Carpenter Custom 465, H1000 (a precipitation-hardened martensitic stainless steel), is developed using an Arbitrary Lagrangian-Eulerian finite-element framework. The model accounts for all the key mechanical and thermal aspects of the process and, as such, is suitable for use in a process-optimization analysis.
2. Since there is no publicly available material model for Carpenter Custom 465, H1000, a thermo-mechanical constitutive model for this material had to be developed, parameterized, and validated. This was accomplished by (a) using all publicly available thermo-mechanical data for this material, (b) employing a material-property correlation procedure, and (c) comparing the computed results for a high-temperature ring-compression test with their experimental counterparts. This approach confirmed that the newly developed thermo-mechanical model for Carpenter Custom 465, H1000, can reasonably account for the mechanical response of this material under high-temperature and high-contact-pressure conditions, the type of conditions encountered in the LFW process.
3. Application of the LFW process model clearly revealed the effect of the key process parameters such as reciprocation frequency, reciprocation amplitude, and the contact pressure on the spatial distribution and temporal evolution of the temperature and the flow fields within the weld.



4. The resulting thermal and flow fields are used within a weld-microstructure module to predict the spatial distribution of the precipitate size over the contact surface. The predicted results are found to be in decent agreement with their experimental counterparts.

## Acknowledgments

The initial portion of the work presented in the current manuscript was supported by the Army Research Office (ARO) through the grant W911NF-11-1-0207. The authors are indebted to Dr. Ralph A. Anthenien, Jr. of ARO for his continuing support and interest in the present work. The authors would also like to thank Dr. David Bowden for helpful discussions and encouragement.

## References

1. A. Vairis and M. Frost, High Frequency Linear Friction Welding of a Titanium Alloy, *Wear*, 1998, **217**, p 117–131
2. A. Vairis and M. Frost, On the Extrusion Stage of Linear Friction Welding of Ti-6Al-4 V, *J. Mater. Sci. Eng. A*, 1999, **271**, p 477–484
3. A. Vairis and M. Frost, Modeling the Linear Friction Welding of Titanium Blocks, *J. Mater. Sci. Eng. A*, 2000, **292**, p 8–17
4. M. Corzo, Y. Torres, M. Anglada, and A. Mateo, Fracture Behaviour of Linear Friction Welds in Titanium Alloys, *Anales de la Mecánica de Fractura*, 2007, **1**, p 75–80
5. O. Roder, J.-P. Ferte, E. Gach, J. Mendez, M. Anglada, and A. Mateo, Development and Validation of a Dual Titanium Alloy Dual Microstructure BLISK, *Fifth Aeronautic Days 2006*, Vienna, Austria, June 2006
6. P. Wanjara and M. Jahazi, Linear Friction Welding of Ti-6Al-4 V: Processing, Microstructure, and Mechanical-Property Inter-Relationships, *Metall. Mater. Trans. A*, 2005, **36**, p 2149–2164
7. W.Y. Li, T.J. Ma, Y. Zhang, Q.Z. Xu, J.L. Li, S.Q. Yang, and H.L. Liao, Microstructure Characterization and Mechanical Properties of Linear Friction Welded Ti-6Al-4 V Alloy, *Adv. Eng. Mater.*, 2008, **10**, p 89–92
8. M. Karadge, M. Preuss, C. Lovell, P.J. Withers, and S. Bray, Texture Development in Ti-6Al-4 V Linear Friction Welds, *J. Mater. Sci. Eng. A*, 2007, **459**, p 182–191
9. M. Karadge, M. Preuss, P.J. Withers, and S. Bray, Importance of Crystal Orientation in Linear Friction Joining of Single Crystal to Polycrystalline Nickel-Based Superalloys, *J. Mater. Sci. Eng. A*, 2008, **491**, p 446–453
10. W.Y. Li, T.J. Ma, Q.Z. Xu, S.Q. Yang, Y. Zhang, J.L. Li, and H.L. Liao, Effect of Friction Time on Flash Shape and Axial Shortening of Linear Friction Welded 45 Steel, *Mater. Lett.*, 2008, **62**, p 293–296
11. T.J. Ma, W.Y. Li, Q.Z. Xu, Y. Zhang, J.L. Li, S.Q. Yang, and H.L. Liao, Microstructure Evolution and Mechanical Properties of Linear Friction Welded 45 Steel Joint, *Adv. Eng. Mater.*, 2007, **9**, p 703–707
12. P. Threadgill, *Linear Friction Welding, TWI, Knowledge Summary*, The Welding Institute, UK, 2008
13. I. Bhamji, M. Preuss, P.L. Threadgill, R.J. Moat, A.C. Addison, and M.J. Peel, Linear Friction Welding of AISI, 316L Stainless Steel, *Mater. Sci. Eng. A*, 2010, **528**, p 680–690
14. L. D'Alvise, E. Massoni, and S.J. Walløe, Finite Element Modeling of the Inertia Friction Welding Process Between Dissimilar Materials, *J. Mater. Process. Technol.*, 2002, **125–126**, p 387–391
15. J. Sorina-Müller, M. Rettenmayr, D. Schneefeld, O. Roder, and W. Fried, FEM Simulation of the Linear Friction Welding of Titanium Alloys, *Comput. Mater. Sci.*, 2010, **48**, p 749–758
16. M. Grujicic, A. Arakere, B. Pandurangan, C.-F. Yen, and B.A. Cheeseman, Process Modeling of Ti-6Al-4 V Linear Friction Welding (LFW), *J. Mater. Eng. Perform.*, 2012, **21**, p 2011–2023
17. A. Midha and D.E. Wert, “Custom 465 Stainless Sees Increased Use in a Wide Array of New and Existing Applications,” <http://www.cartech.com/news.aspx?id=4262>. Accessed on January 29, 2014
18. M. Grujicic, S. Tangirala, B.O. Cavin, W.D. Porter, and C.R. Hubbard, Effect of Iron Additions on Structure of Laves Phases in Nb-Cr-Fe Alloys, *Mater. Sci. Eng.*, 1993, **A160**, p 37–48
19. Technical datasheet for Carpenter Custom 465, <http://cartech.ides.com/datasheet.aspx?I=101&E=55>. Accessed on Jan 29, 2014
20. M. Grujicic, G. Arakere, B. Pandurangan, A. Hariharan, C.-F. Yen, B.A. Cheeseman, and C. Fountzoulas, Statistical Analysis of High-Cycle Fatigue Behavior of Friction Stir Welded AA5083-H321, *J. Mater. Eng. Perform.*, 2011, **20**, p 855–864
21. M. Grujicic, G. Arakere, A. Hariharan, and B. Pandurangan, A Concurrent Product-Development Approach for Friction-Stir Welded Vehicle-Underbody Structures, *J. Mater. Eng. Perform.*, 2012, **21**, p 437–449
22. M. Grujicic, G. Arakere, A. Hariharan, and B. Pandurangan, Two-Level Weld-Material Homogenization Approach for Efficient Computational Analysis of Welded Structure Blast Survivability, *J. Mater. Eng. Perform.*, 2012, **21**, p 786–796
23. M. Grujicic, G. Arakere, B. Pandurangan, J.M. Ochterbeck, C.-F. Yen, B.A. Cheeseman, A.P. Reynolds, and M.A. Sutton, Computational Analysis of Material Flow During Friction Stir Welding of AA5059 Aluminum Alloys, *J. Mater. Eng. Perform.*, 2012, **21**, p 1824–1840
24. M. Grujicic, B. Pandurangan, C.-F. Yen, and B.A. Cheeseman, Modifications in the AA5083 Johnson-Cook Material Model for Use in Friction Stir Welding Computational Analyses, *J. Mater. Eng. Perform.*, 2012, **21**, p 2207–2217
25. M. Grujicic, B. Pandurangan, A. Arakere, C.-F. Yen, and B.A. Cheeseman, Friction Stir Weld Failure Mechanisms in Aluminum-Armor Structures under Ballistic Impact Loading Conditions, *J. Mater. Eng. Perform.*, 2013, **22**, p 30–40
26. M. Grujicic, S. Ramaswami, J.S. Snipes, R. Yavari, A. Arakere, C.-F. Yen, and B.A. Cheeseman, Computational Modeling of Microstructure Evolution in AISI1005 Steel during Gas Metal Arc Butt Welding, *J. Mater. Eng. Perform.*, 2012, **22**, p 1209–1222
27. M. Grujicic, A. Arakere, S. Ramaswami, J.S. Snipes, R. Yavari, C.-F. Yen, B.A. Cheeseman, and J.S. Montgomery, Gas Metal Arc Welding Process Modeling and Prediction of Weld Microstructure in MIL A46100 Armor-Grade Martensitic Steel, *J. Mater. Eng. Perform.*, 2013, **22**, p 1541–1557
28. M. Grujicic, S. Ramaswami, J.S. Snipes, C.-F. Yen, B.A. Cheeseman, and J.S. Montgomery, Multi-Physics Modeling and Simulations of MIL A46100 Armor-Grade Martensitic Steel Gas Metal Arc Welding Process, *J. Mater. Eng. Perform.*, 2013, **22**, p 2950–2969
29. M. Awang, V. Mucino, Z. Feng, and S. David, *Thermo-Mechanical Modeling of Friction Stir Spot Welding (FSSW)*, SAE Technical Paper 2006-01-1392, 2006, doi:10.4271/2006-01-1392
30. S.J. Na, J. Ruge, and K. Thomas, Temperature Determination During the Friction Welding of Dissimilar Materials in Cylindrical Form-Measurement and Calculation, *Schweiss. Schneid.*, 1984, **36**, p E43–E45
31. M. Grujicic, C.L. Zhao, and E.C. Dusel, The Effect of Thermal Contact Resistance on Heat Management in the Electronic Packaging, *Appl. Surf. Sci.*, 2005, **246**, p 290–302
32. <http://www.thermalengineer.com/library/ContactResistanceConcept.htm>. Accessed on January 29, 2014
33. ABAQUS Version 6.10-EF1, User Documentation, Dassault Systèmes, 2010
34. G. R. Johnson and W. H. Cook, A Constitutive Model and Data for Metals Subjected to Large Strains, High Strain Rates and High Temperatures, *Proceedings of the 7th International Symposium on Ballistics*, 1983
35. British Stainless Steel Association, Elevated temperature physical properties of stainless steels, <http://www.bssa.org.uk/topics.php?article=139>. Accessed on January 29, 2014
36. K. Park, Development and Analysis of Ultrasonic Assisted Friction Stir Welding Process, Ph.D. dissertation, University of Michigan, 2009
37. W.S. Owen and M. Grujicic, Plastic Deformation: Thermally Activated Glide of Dislocations, *Encyclopedia of Materials Science and Engineering*, Pergamon Press, Oxford, England, p 3540–3543, 1986
38. M. Grujicic, G.B. Olson, and W.S. Owen, Kinetics of Martensitic Interface Motion, ICOMAT-82(International Conference on Martensitic Transformations), *J. Phys. Colloques*, 1982, **43**, p C4-173–C4-178
39. M. Grujicic, I.J. Wang, and W.S. Owen, Precipitate/Austenite Equilibrium in a Titanium-Niobium Ultra-low Carbon Steel, *Calphad*, 1986, **10**, p 117–128
40. M. Grujicic, The Core Structure of  $a/2 < 110 >$  Screw Dislocations in Fe-Ni-Cr-N Austenite, *Mater. Sci. Eng. A*, 1994, **183**, p 223–232
41. M. Grujicic and J. Du, Atomistic Simulations of Transformation Toughening in Fe-Ni Austenite, *Modelling Simul. Mater. Sci. Eng.*, 1995, **3**, p 811–828